AGU100 ADVANCING EARTH AND SPACE SCIENCE

Journal of Advances in Modeling Earth Systems

RESEARCH ARTICLE

10.1029/2018MS001356

Key Points:

- We present an idealized model of the stratosphere and troposphere with actual topography and zonally asymmetric equilibrium temperatures
- Compared to reanalysis, the new model's circulation is more realistic than in previous studies
- The surface momentum damping is important for the model's circulation and controls the frequency of stratospheric sudden warming events

Correspondence to:
Z. Wu,
zheng.winnie.wu@utah.edu

Citation:
Wu, Z., & Reichler, T. (2018). Towards a more Earth-like circulation in idealized models. *Journal of Advances in Modeling Earth Systems*, *10*. https://doi.org/10.1029/2018MS001356

Received 24 APR 2018
Accepted 12 JUN 2018
Accepted article online 19 JUN 2018

Towards a More Earth-Like Circulation in Idealized Models

Zheng Wu[1] and Thomas Reichler[1]

[1]Department of Atmospheric Sciences, University of Utah, Salt Lake City, UT, USA

Abstract Idealized models are useful for the investigation of dynamical phenomena in which physical processes play a secondary role. Typically, such models employ highly idealized topography and zonally symmetric equilibrium temperatures as forcings. However, these simplifications are somewhat unrealistic and make these models unfit for investigations in which similarity with the real atmosphere is crucial. In this study, we present a new idealized model of the stratosphere-troposphere system which has a more Earth-like circulation than previous models. We accomplish this by introducing into the dry dynamical core of the Geophysical Fluid Dynamics Laboratory realistic topography and equilibrium temperatures with zonal asymmetries. We then explore the model's sensitivity to the prescribed strength of the surface momentum drag. We find improvements in the model's circulation when validating against reanalysis. Most notably, the strength and structure of the winds, the spectrum of planetary waves, and the frequency of stratospheric sudden warming events are more realistic than in traditional idealized models. In the extratropics, the diagnosed diabatic forcing of the model also compares favorably against the observations. We further find that variations in the surface momentum damping exert an important control on the model's circulation, including the frequency of stratospheric sudden warming events. We believe that the new model reduces the gap between traditional idealized models and full models and that it is useful for the investigation of phenomena in which greater similarity with the real system is needed. The code for the new model and its equilibrium temperature data set is published on GitHub.

1. Introduction

Idealized general circulation models are popular tools for the study of atmospheric dynamics. Idealized models solve the primitive equations by nudging the temperatures toward prescribed equilibrium temperatures to represent diabatic heating, essentially isolating the dynamics from the complicated physical parameterizations. Idealized models are simple and easy to use, and their low computational cost allows intensive studies of parameter sensitivities. Since Held and Suarez (1994, hereafter HS94) proposed a basic setup for this class of models, a number of follow-up studies extended such models into the stratosphere (Jucker et al., 2013, 2014; Kushner & Polvani, 2004; Polvani & Kushner, 2002; Reichler et al., 2005).

The reason behind the extension of models into the stratosphere is an increasing interest in stratospheric dynamics, in particular in stratospheric sudden warming events (SSWs). SSWs are extreme circulation phenomena of the northern hemispheric winter stratosphere, characterized by sudden increases of temperatures and breakdowns of the stratospheric polar vortex (Mcintyre, 1982). The interest in SSWs is related to the dynamical coupling between the stratosphere and troposphere and the realization that SSWs are a key ingredient for the coupling. In other words, SSWs have important and long-lasting impacts on surface weather and climate (Baldwin & Dunkerton, 2001; Thompson et al., 2002). SSWs are mostly phenomena of atmospheric dynamics, and the radiative relaxation time scale also plays a role (Hitchcock et al., 2013). Therefore, idealized models are well suited to study SSWs, as also reflected by the large number of previous studies that employed such models to understand SSW dynamics.

Matsuno (1971) showed that SSWs are primarily caused due to the interaction of the polar vortex with planetary waves, which originate from the lower atmosphere and propagate upward into the vortex region. Consequently, planetary waves are a prerequisite for the occurrence of SSWs (Charlton et al., 2007; Polvani & Waugh, 2004). Topography is an important factor for the generation of such waves (Chen & Trenberth, 1988; Held et al., 2002), and several idealized modeling studies have investigated the effect of topography on the occurrence of SSWs (Gerber & Polvani, 2009; Jucker et al., 2014; Sheshadri et al., 2015). These studies found that in order to create a sufficient number of SSWs, a wave-2 sinusoidal topography with a peak-to-trough difference of 6,000 m is ideal. Conversely, Wu and Smith (2016) found that an Earth-like topography alone does not produce sufficient planetary waves and number of SSWs. Therefore, studies of stratospheric dynamics with idealized models require a topography with an unrealistically large amplitude. However, we believe that for certain studies this is an important limitation because actual topography is crucial for the generation of a realistic spectrum of planetary waves.

Idealized models are also limited by their lack of zonal asymmetries in the equilibrium temperatures and thus in the diabatic forcing of the flow. Realistic zonal asymmetries in the diabatic forcing are essential for creating the thermal contrast between land and ocean, which besides topography is another important forcing mechanism for planetary waves (Held et al., 2002). This also explains why previous studies needed topography with a very large amplitude, as the zonally symmetric equilibrium temperatures did not produce enough planetary waves for the generation of SSWs.

Another uncertainty of idealized models is the momentum damping in the planetary boundary layer. Chen et al. (2007) found that the damping rate is important for the latitudinal position of the tropospheric jet, in the sense that increasing the damping moves the jet equatorward. There is reason to believe that the meridional alignment of the circulation with the topography, which among other things depends on the damping, influences the planetary waves and their interaction with the polar vortex (Limpasuvan & Hartmann, 2000). Most of the previous studies followed the surface damping rate given by HS94, which at the surface is 1 d^{-1}. But given the crucial influence of the damping rate on the simulated circulation, the choice of the rate needs to be reconsidered carefully.

The goal of the present study is to overcome some of the limitations and uncertainties of previous studies by introducing actual topography and zonally asymmetric equilibrium temperatures into an idealized model. As we will show, the two changes combined lead to a circulation that is much more realistic than in former studies. We then use the new model to perform a parameter sweep experiment, using different values of the momentum damping at the surface, and study the sensitivity of the coupled stratosphere-troposphere system to the damping.

The paper is organized as follows. In section 2, we describe the setup of our model and the numerical experiments. In section 3, we present the analysis of our experiments, with a particular emphasis on the improved stratospheric and tropospheric circulation and frequency of SSWs. Finally, section 4 gives a conclusion and discussion.

2. Model Description and Numerical Experiments

2.1. Model Setup

We use the Geophysical Fluid Dynamics Laboratory (GFDL) spectral dynamical core at a horizontal resolution of T42 (Polvani & Kushner, 2002). The model has 40 vertical σ levels between the surface and 0.01 hPa. Linear Rayleigh damping of the low-level winds is used to mimic frictional effects in the boundary layer. Temperatures T are nudged by Newtonian relaxation toward prescribed radiative equilibrium temperatures T_{eq}, that is,

$$\frac{\partial T}{\partial t} = -\frac{T - T_{eq}}{\tau}, \quad (1)$$

where τ is the prescribed relaxation time scale. Throughout this study, the T_{eq} fields are determined individually for each month of the year, and linear interpolation is used to prescribe daily varying values to the model. We start our experiments using an analytically determined T_{eq} profile given in the appendix of Jucker et al. (2014, hereafter JFV14). This initial profile, which we denote as $T_{eq(0)}$, is a function of latitude, height, and time, and it can be easily modified through parameters. Compared to earlier studies, the JFV14 formulation for T_{eq} substantially improves the stratospheric wind and temperature structure and allows more planetary wave fluxes to reach the stratosphere. The time scale τ in (1) is also taken from JFV14 and is kept the same for all our experiments.

Our initial $T_{eq(0)}$ is zonally symmetric. However, as discussed in the introduction, zonal variations in diabatic heating, which in our model are related to zonal variations in T_{eq}, are important for creating stationary waves and for the wave forcing of the stratosphere (Becker & Schmitz, 2003). In contrast to earlier studies with idealized models, we therefore optimize T_{eq} by introducing zonal asymmetries into it. This is achieved by following the iterative procedure by Chang (2006). The iteration consists of N steps. During each step, we use a fixed

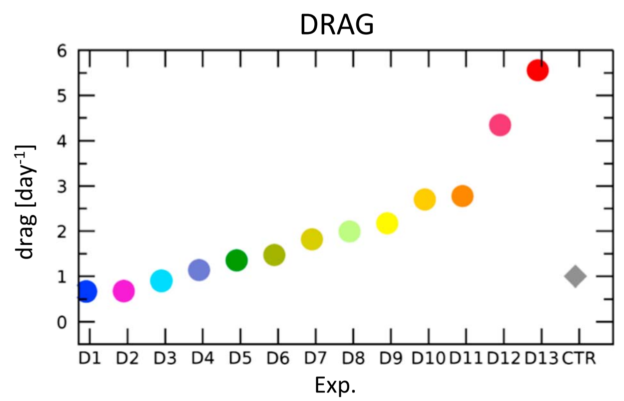

Figure 1. Surface drag (d^{-1}) for the DRAG (colored circles) and CTR (gray diamond) experiments.

T_{eq}, named $T_{eq(N)}$, and run the model for Y years. We then calculate the three-dimensional model simulated temperature climatology $\overline{T_{(N)}}$, compare it on pressure levels against the corresponding climatology $\overline{T_R}$ from the second Modern-Era Retrospective analysis for Research and Applications (Bosilovich et al., 2016), and correct T_{eq} for the next iteration step $N + 1$ according to

$$T_{eq(N+1)} = T_{eq(N)} - \frac{2}{3}\left(\overline{T_{(N)}} - \overline{T_R}\right), N = 1, 2, 3, \dots \quad (2)$$

The factor of 2/3 follows Chang (2006) to avoid overcorrection, overbars indicate climatological averages, and all fields are calculated individually for each month of the year. The result of the iteration is that zonal asymmetries are added into T_{eq} and that the simulated temperature climatology converges toward that of the reanalysis. Note that using $\overline{T_R}$ as T_{eq} would create a zero forcing in the mean if the model's temperature climatology would be the reanalysis climatology. Thus, $\overline{T_R}$ is inadequate as a forcing for the model.

The lower boundary of our model is formed by the actual Earth topography, taken from the GFDL AM2.1 climate model (Anderson et al., 2004). This topography allows for the generation of more realistic planetary waves than in models with sinusoidal topography.

2.2. Numerical Experiments

In idealized models, the horizontal winds in the boundary layer are typically damped by Rayleigh friction following HS94. Mathematically, this can be written by

$$\frac{\partial v}{\partial t} = \dots - k_v(\sigma)v, \quad (3)$$

where v is the wind and σ is the model's vertical sigma level p/p_s. In (3), k_v is the damping rate, following the form in HS94 as

$$k_v = k_f \max\left(0, \frac{\sigma - \sigma_b}{1 - \sigma_b}\right), \quad (4)$$

where k_f is the surface damping rate and $\sigma_b = 0.7$. Thus, the damping rate k_v decreases linearly with height, from a prescribed surface value k_f to a value of zero at $\sigma = 0.7$ and above. We denote k_f as the surface drag.

We perform a number of numerical experiments with our model, using different strengths of the surface drag. We denote these experiments as DRAG experiments. In total, we perform 13 experiments (D1 … D13), with their surface drag shown in Figure 1. Simulation D1 has the smallest, and D13 has the largest drag. Most experiments consist of $N = 31$ iterations, ensuring that T_{eq} converges toward a stable solution and a temperature climatology that resembles the reanalysis. D1, D2, D4, and D8 start from an already equilibrated T_{eq} taken from D3, necessitating less iterations for convergence. Each iteration is run for $Y = 30$ years, except for the last two iterations ($N = [30, 31]$), which are run for 201 and 501 years, respectively, to improve our final statistical analysis.

In order to put our results into perspective, we also perform a 501-yearlong control run (denoted by CTR). T_{eq} for CTR follows the simulation 3 formulation given by JFV14. CTR does not undergo the iterative procedure described above, has an analytical T_{eq} without zonal asymmetries, and uses a wave-2 sinusoidal topography with a 3-km amplitude centered at 45°N. There is only one difference between our CTR and JFV14 simulation 3: We add a seasonal cycle to CTR by calculating monthly values following Jucker et al. (2014, equations (A12)–(A15)), which are then interpolated to daily values. In contrast, the original JFV14 simulation is run in a perpetual January mode.

2.3. Data Analysis

Most of our analysis is carried out for January-February-March (JFM) means, and most variables are latitude-weighted averages from 20°N to 90°N, considering all levels from 1,000 to 1 hPa, unless otherwise specified.

In calculating climatologies, we discard from each iteration the first year as spin-up and focus our analysis on the remaining 500 years. The climatologies of our experiments are validated against the ERA-40 reanalysis (1958–2001; Uppala et al., 2005).

Our definition of SSWs is similar to the criterion of Charlton and Polvani (2007), considering a reversal of the daily zonal-mean zonal wind at 10 hPa and 60°N. Two wind reversals in the same season are treated as distinct SSWs if they are separated by at least 43 days. Based on the National Centers for Environmental Prediction/National Center for Atmospheric Research (NCEP/NCAR) reanalysis (NNR; Kalnay et al., 1996) over the period 1948–2015, we find an observation-based climatological SSW frequency $\hat{p}$ of 0.53 events per year. In calculating the confidence interval of $\hat{p}$, we assume that SSWs are independent Bernoulli trials and neglect the possibility of multiple SSWs per year (in NNR, this occurs only in 5 out of the 36 years with SSWs). Then, the approximate confidence interval is given by

$$\hat{p} \pm z_{1-\frac{\alpha}{2}} \cdot \sqrt{\frac{\hat{p}(1-\hat{p})}{n}}, \tag{5}$$

where $z_{1-\frac{\alpha}{2}}$ is the $1-\frac{\alpha}{2}$ quantile of a standard normal distribution, $\alpha = 0.05$ is the target error rate, and $n = 68$ is the number of years of the NNR. With this, the 95% confidence interval of the yearly SSW frequency in the NNR is 0.41–0.65.

We follow the Baldwin and Dunkerton (2001) definition of the northern annular mode (NAM). The spatial NAM pattern at each pressure level is the first empirical orthogonal function of daily data from January to March of the 500-year zonal mean geopotential height anomalies north of 20°N. The anomalies are calculated with respect to the daily varying climatology.

We employ Eliassen-Palm (EP) flux diagnostics (Eliassen & Palm, 1961) to analyze wave-mean flow interaction. More specifically, we calculate the horizontal and vertical component of the quasi-geostrophic version of the EP-flux vector **F** (Edmon et al., 1980) in pressure coordinates. For a graphical display, we scale the horizontal and vertical vectors by $\frac{\frac{1}{a}\cos\varphi}{\pi}$ and $\frac{\cos\varphi}{10^5\,\mathrm{Pa}}$ (a is the radius of the Earth, while φ is latitude), respectively. Both vectors are also scaled by a factor of $\sqrt{\frac{1{,}000}{p}}$ (p is pressure). Vertical vectors above 100 hPa are additionally multiplied by a factor of 6.0 for clarity.

We use observation-based estimates of the climatological three-dimensional distribution of the diabatic heating rate Q, determined by Chan and Nigam (2009) as the residual in the thermodynamic equation based on ERA-40 reanalysis.

3. Results

3.1. Error Evolution by Iteration

To evaluate our simulations and iterations and to identify which value for the surface drag parameter is best, we study simulation errors with respect to the ERA-40 reanalysis for six quantities (Figure 2). The quantities are the NH climatological JFM (a) tropospheric temperature, (b) stratospheric temperature, (c) tropospheric zonal wind, (d) stratospheric zonal wind, (e) latitude-pressure cross section (20–90°N, 1,000–1 hPa) of the NAM pattern, and (f) the SSW frequency $\hat{p}$. Here tropospheric refers to 1,000–200 hPa and stratospheric to 100–1 hPa. Our choice of quantities was motivated by an interest in the dynamical coupling between the stratosphere and the troposphere. In each panel, the columns are for the different experiments and the rows are for the various iterations, with the first iteration at the top and the last iteration at the bottom. The shading in each grid box indicates the error.

Going from top to bottom, the errors generally decrease with increasing iteration number. This reduction can be seen in almost all quantities, indicating that improving the temperatures in an idealized model generally leads to improved simulations of the atmospheric circulation. The general reduction in errors with iteration also demonstrates the success of our iterative procedure in achieving a more realistic Earth-like circulation. This becomes particularly clear by comparing the errors for the last iteration of our DRAG experiment with that of the CTR experiment (last column, bottom).

The relative reduction in error is larger for temperature (factor 6, from initially 6 to 1 K) than for the zonal wind (factor 3, from 9 to 3 m/s in the troposphere and from 15 to 5 m/s in the stratosphere) and for the other

10.1029/2018MS001356

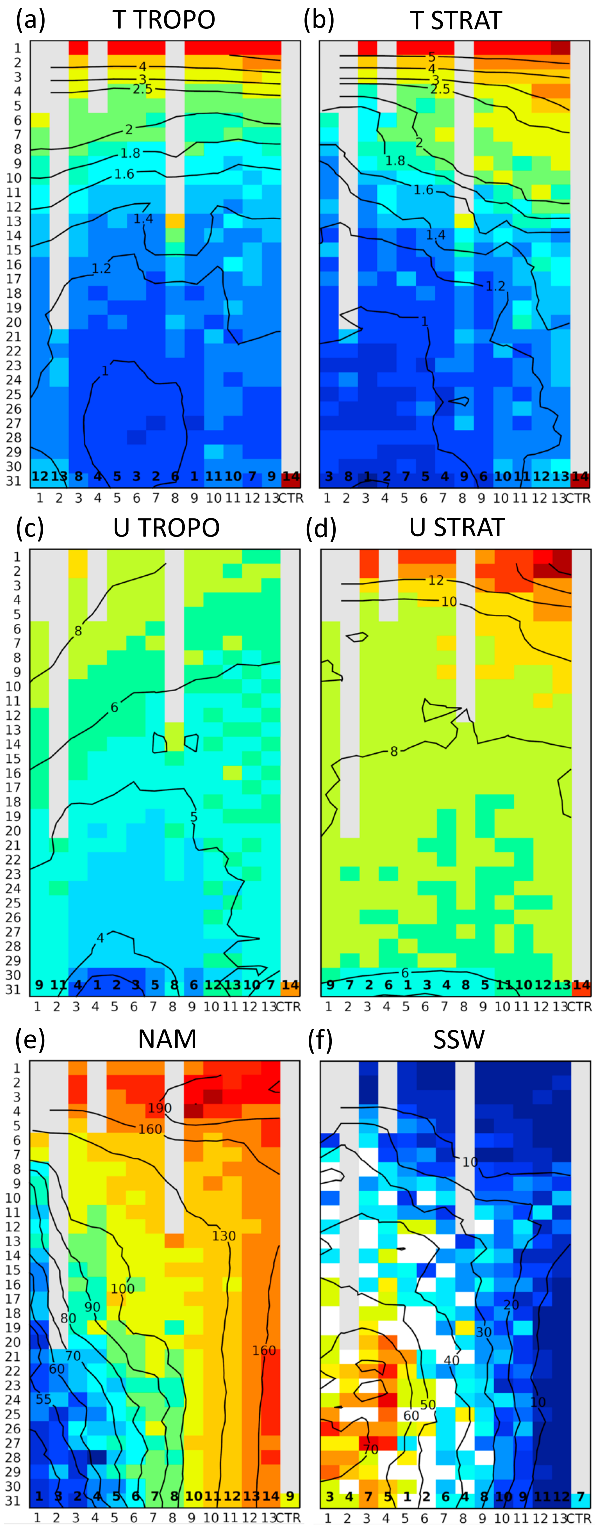

Figure 2. Climatological errors during January-February-March with respect to reanalysis. The colors and contours show the same information, with color bars omitted for simplicity. Shown are (a) tropospheric (1,000–200 hPa) temperature (in K), (b) stratospheric (100–1 hPa) temperature, (c) tropospheric (1,000–200 hPa) zonal wind (in m/s), and (d) stratospheric (100–1 hPa) zonal wind, (e) northern annular mode pattern (20–90°N, 1,000–1 hPa) (in m), and (f) stratospheric sudden warming (SSW) frequency $\widehat{p}$ (in events per 100 years, or %). (a)–(d) are three-dimensional (longitude, latitude, and pressure) northern hemispheric root-mean-square (RMS) differences with respect to ERA-40, (e) is a two-dimensional (latitude-pressure) RMS difference, and (f) shows the actual SSW frequency. The white shading in (f) indicates that the SSW frequency is within the 95% confidence interval of the NCEP/NCAR reanalysis (1948–2015), which is 41–65%. Numbers for iteration 31 indicate the experiment ranking for each quantity, with 1 being the best.

quantities. The fact that the error reduction is slower for the zonal wind and that it continues beyond apparent reductions in temperature suggests that the zonal wind is not only determined by the thermal wind relationship. Subtle nongeostrophic effects, like wave-mean flow interaction or changes in surface drag, are also important. The reduction in error is also not strictly monotonic with iteration, suggesting that the 30-yearlong climatological means of each iteration are perhaps somewhat short relative to the internal variability. The last two iterations (30 and 31) are much longer (200 and 500 years, respectively) and therefore show much reduced errors for the zonal wind. It is also of note that the errors in zonal wind are larger in the stratosphere than in the troposphere, probably because of the overall larger wind speeds and internal variability in the stratosphere. The error reduction for the NAM pattern is relatively slow, with some experiments showing almost no improvement by iteration. The evolution of the frequency of SSWs (Figure 2f) deserves some extra discussion. We note first that the outcomes from iteration to iteration for the same experiment are quite variable. This reflects the fact that SSWs are rare events, that the frequency is affected by considerable internal variability, and that the 30-yearlong period is relatively short for deriving reliable estimates of the frequency. The large internal variability and slow convergence of the SSW frequency was also one of our main reasons to conduct a relatively large number of iterations (31) and increase the length of the last two iterations (from 30 to 200 and 500, respectively).

Another point of interest is that the magnitude of the surface drag has a significant influence on the climatological NAM pattern and frequency of SSWs. In other words, the surface drag influences the tropospheric internal variability and the nature of the coupling between the stratosphere and troposphere. Experiments with large surface drag (D8–D13) tend to have large NAM errors and a much-reduced SSW frequency (5%), while experiments with smaller drag (D1–D4) have a NAM pattern that is similar to that of the reanalysis and a SSW frequency that is too high (up to 80%) compared to the reanalysis. Note that this influence of the surface drag is despite similar and small errors in the simulation of temperature and wind across the 13 experiments. We also note that for certain experiments (D5–D6), the frequency of SSWs is very similar to the observations, despite the use of a realistic topography in our idealized model setup. This is in contrast to most previous studies, which had to use unrealistically large amplitude bottom topography to generate sufficient planetary wave forcing and number of SSWs.

Going from experiment to experiment for the last iteration, it seems difficult to determine which of the 13 DRAG experiments is overall the best. The temperature and wind errors are smallest for experiments D3–D9, but the NAM pattern seems to be most realistic for experiment D1–D3, and the SSW frequency is closest to that of the reanalysis for experiments D5–D6. Considering the overall performance, especially for the NAM pattern, we estimate that D3 (surface drag = 0.9 d^{-1}) is one of the most realistic and D13 (surface drag = 5.6 d^{-1}) is the least realistic experiment. Note that D5 is also quite realistic, in particular in terms of SSW frequency and zonal wind structure. But in our subsequent analysis, we prefer D3 over D5 because of D3's more realistic NAM pattern, which we believe is important for the downward coupling between the stratosphere and troposphere.

3.2. Climatological Circulation

We now compare the observed climatological winter circulation from the reanalysis with that from our "best" experiment D3 and the "baseline" CTR experiment. Figure 3 shows the JFM climatologies for ERA-40 and the differences of D3 and CTR with respect to ERA-40. The improvements of D3 over CTR are most evident in terms of temperature (first row), with the RMS errors with respect to the reanalysis over the northern hemisphere being ~10 times larger for CTR than for D3 (see numbers at top). The improved temperature structure of D3 over CTR is also reflected in the zonal wind (second row), but perhaps to a lesser extent than one would expect from the small D3 temperature error. In terms of the RMS error, there is about a fourfold decrease in D3 over CTR, with the overall configuration of the tropospheric jet and the polar vortex in D3 being more realistic than in CTR. The stratospheric wind biases of D3 can be best described by a polar vortex that is too weak, which is also consistent with the somewhat too high SSW frequency seen in this experiment (Figure 2f). In contrast, CTR shows a tilted and equatorward shifted polar vortex and a poleward shifted tropospheric jet.

Figure 3c compares the full fields of the climatological zonal wind in the horizontal plane at 500 hPa. As in our new model the orography and the land-sea temperature contrast is quite realistic, D3 successfully reproduces the observed strength, location, and tilt of the North Pacific and North Atlantic jets. This is similar to the improvements shown in Chang (2006). CTR also exhibits two wind maxima, but predictably, they are entirely symmetric, and roughly aligned with the location of the minima of CTR's wave-2 topography.

The structure and magnitude of the NAM pattern over the northern hemisphere (Figure 3d) in D3 compare favorably against the reanalysis, except that the positive lobe of the NAM over the lower latitudes is perhaps somewhat too strong. On the other hand, in CTR the NAM pattern is clearly too weak and has a different structure from that in the reanalysis.

Previous papers indicated that the horizontal wind shear (Dickinson, 1968) and the position of the tropospheric westerlies (Limpasuvan & Hartmann, 2000) guide the upward propagation of planetary waves. Other studies showed an influence of the tropospheric jet structure on the eddy-zonal flow interaction (Eichelberger & Hartmann, 2007) and an effect of the tropospheric jet latitude on the coupling between stratosphere and troposphere (Garfinkel & Waugh, 2014). Therefore, the configuration of the tropospheric jet and polar vortex may have important influences on the strength and propagation of the planetary waves. This issue is investigated in Figure 3e, showing cross sections of the EP-flux and its divergence. The two panels for D3 and CTR are actual differences with respect to ERA-40. Overall, the strength of the upward propagating waves in D3 matches more closely the ERA-40 than CTR. The tropospheric EP-flux differences for D3 suggest a somewhat too small and poleward displaced planetary wave propagation, whereas the differences in the stratosphere are mostly small. In contrast, CTR shows a too strong and equatorward shifted wave propagation in the troposphere and much reduced upward propagation in the polar atmosphere except the upper stratosphere. The equatorward bending of the waves seen in the upper stratosphere for the ERA-40 is also insufficient in CTR, but it is about right in D3. Similar improvements can also be seen in terms of the EP-flux divergence (shading), but with weaker magnitude. Closer inspection of D3 shows a negative EP-flux divergence anomaly in the lower stratosphere, which is consistent with the too weak polar vortex (Figure 3b) and perhaps indicative for more frequent SSWs than in the observations.

In Figure 4a, we compare the JFM climatological meridional heat flux at 100 hPa for ERA-40, our best experiment D3, our worst experiment D13, and the control experiment CTR. The figure shows the stationary and transient heat flux by wave number. For the CTR experiment (gray), both the stationary and transient heat

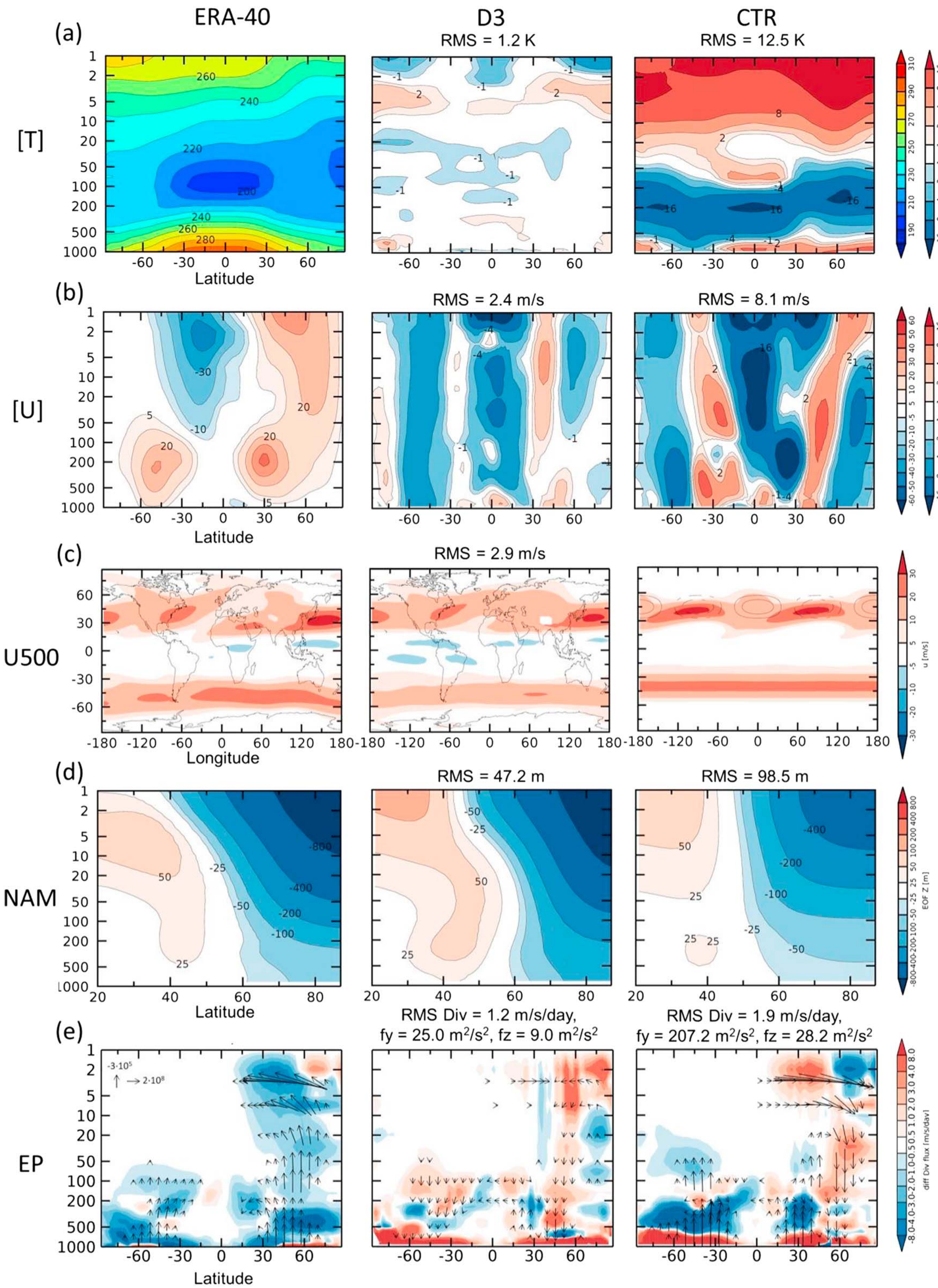

Figure 3. January-February-March climatologies. Shown are (a) zonal-mean temperature (in K), (b) zonal-mean zonal wind (in m/s), (c) horizontal zonal wind at 500 hPa (in m/s), (d) northern annular mode pattern (20°–90°N; in m), and (e) Eliassen-Palm (EP) flux vectors (arbitrary scaling) and (shading) EP-flux convergence (m/s/d). (left) Full fields from ERA-40 and (middle and right) differences with respect to ERA-40, except for (c) and (d), which show full fields for D3 and CTR. In (e), only EP-flux (vectors) exceeding 14 $m^2\,s^{-2}$ (after scaling) are shown; the two scaling vectors on the top left for ERA-40 have (unscaled) lengths of $2 \cdot 10^8$ m^3/s^2 (meridional) and $-3 \cdot 10^5$ kg m/s^4 (vertical); differences have been multiplied by 2 in the middle and right panel. Numbers on top of each panel are area averaged root-mean-square (RMS) errors over the northern hemisphere (20°–90°N, 1,000–1 hPa). In (e), the numbers on top show area averaged RMS errors at 100–1 hPa, and errors for the vector components are calculated after the scaling.

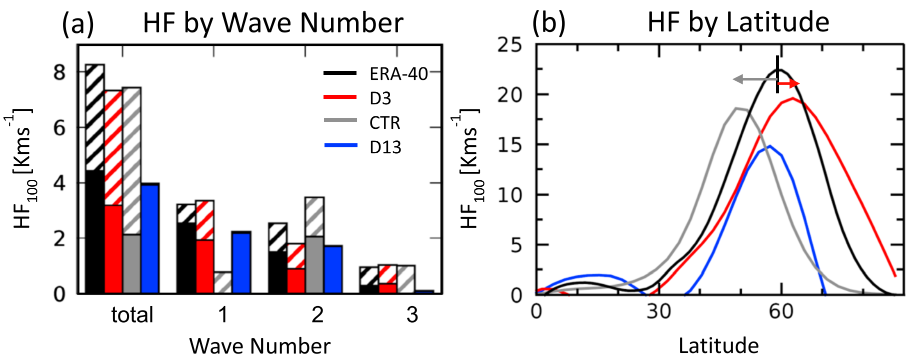

Figure 4. Meridional heat fluxes at 100 hPa. Shown are (a; solid) stationary and (hatched) transient heat fluxes (20°–90°N) by wave number and (b) total heat flux by latitude. Stationary components are based on climatological fields and represent deviations from the zonal mean; transient components are based on daily data and represent deviations from the zonal mean minus the stationary component.

fluxes are dominated by their wave-2 components, which makes sense given the orographic forcing of this experiment. In contrast, the two DRAG experiments D3 (red) and D13 (blue) display more realistic stationary heat fluxes than CTR, demonstrating the usefulness of our experimental design for achieving an Earth-like planetary wave spectrum. With relatively small drag (D3), both the stationary and transient heat flux components are similar to the reanalysis, while in the large drag experiment (D13), the transient heat flux is almost completely suppressed. The variation in stationary heat fluxes is small across our DRAG experiments (not shown) since they all use the same realistic topography and are designed to reproduce reanalysis-like temperatures. However, the transient heat fluxes are under the large influence of surface drag and vary considerable among the experiments. The success of D3 in having quite realistic transient heat fluxes is perhaps somewhat surprising, since there is no guarantee that a good climatological circulation also produces realistic transients. D3 has a similar total heat flux as CTR, even though D3's bottom topography is by far not as high as in CTR. This is also consistent with the EP-fluxes shown in Figure 3e, indicating the importance of zonal asymmetries in T_{eq} for generating planetary waves.

Figure 4b shows the latitudinal distribution of the total heat flux over the Northern Hemisphere. For ERA-40, the maximum of the total heat flux is located near 60°N. Compared to ERA-40, the total heat flux in D3 (red) is somewhat shifted poleward, and that of D13 (blue) and CTR (gray) are shifted equatorward. Similar displacements can be seen in terms of the EP-fluxes in Figure 3e. These shifts bear resemblance with Chen et al. (2007), who found that increasing (decreasing) surface drag tends to shift the westerlies equatorward (poleward).

In Figure 2f, if we focus on how the SSW frequency varies by experiment for the last iteration (31), we find that increasing surface drag tends to reduce the number of SSWs. This is consistent with the reduction of the heat fluxes with increasing drag seen in Figure 4a and knowing that the enhanced upward propagation of wave activity, as indicated by the heat fluxes, is the root cause for SSWs (Matsuno, 1971). However, the outcomes for experiment CTR in Figure 2f also make it clear that having a realistic heat flux magnitude alone does not guarantee a realistic SSW frequency: Compared to the reanalysis, CTR has similar heat fluxes but not enough SSWs (33%). Possible reasons for this could be the equatorward displacement of the heat fluxes and/or a stronger vortex (Figure 3b) in CTR, possibly leading to less effective wave-mean flow interaction, or the fact that the heat fluxes are almost entirely concentrated on wave-2 in CTR.

3.3. Diabatic Heating Rate

In this section, we analyze the effective diabatic heating rate Q of our idealized model, given by

$$Q = \frac{T_{eq} - \overline{T}}{\tau}, \tag{6}$$

where $\overline{T}$ is the model simulated climatological temperature and the other quantities are as explained in the methodology. Since our T_{eq} is chosen such as to create model temperatures $\overline{T}$ that resemble the reanalysis, Q should also resemble the reanalysis if the model's circulation and its associated adiabatic heating and heat

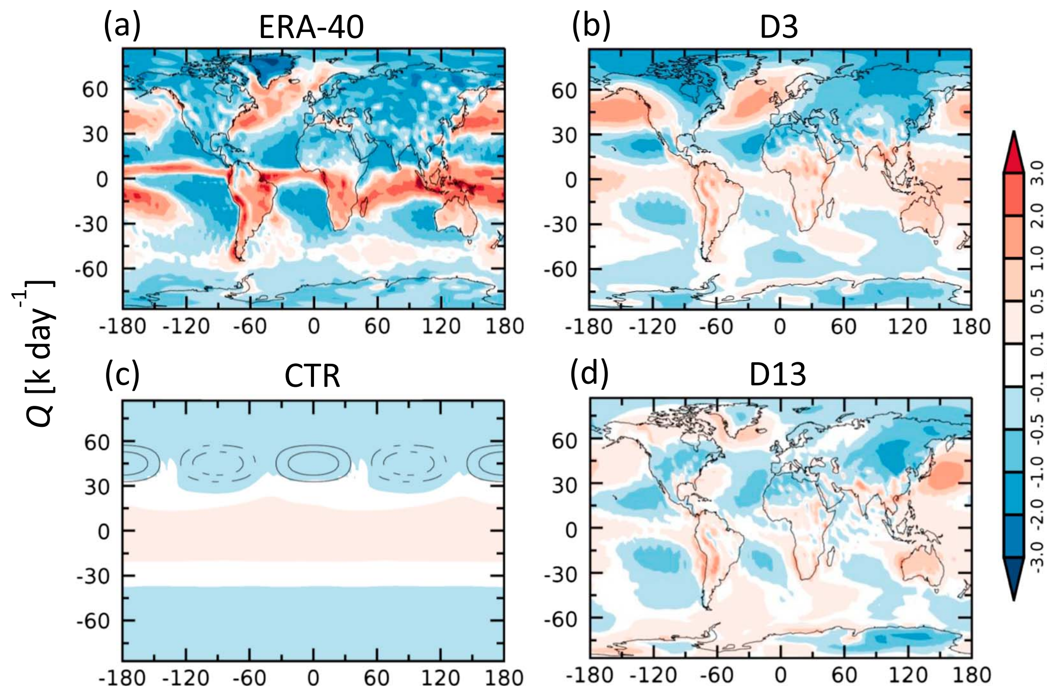

Figure 5. Diabatic heating rate Q (in K/d) in January. Shown is vertically mass weighted average (surface to 150 hPa) of Q for (a) reanalysis and (b–d) three experiments. Contours are at ±(0.1, 0.5, 1, 2, 3, 4) K/d.

transports are realistic. Figure 5 compares the vertically averaged (surface to 150 hPa) Q in January between the ERA-40 reanalysis and the experiments D3, D13, and CTR. To very first order, all three experiments tend to have positive Q in the tropics and mostly negative Q everywhere else. This is similar to the reanalysis and consistent with the global distribution of the radiative energy fluxes. However, closer inspection reveals significant and important differences in the patterns of Q among the three experiments.

In the northern extratropics, the patterns of Q in D3 (Figure 5b) are quite similar to the reanalysis (Figure 5a). Most importantly, the position and strength of the heating associated with the latent heat release of the North Pacific and North Atlantic storm tracks are well reproduced in D3. The cooling over the remaining extratropical regions is also well captured by D3. Major discrepancies between D3 and the reanalysis exist over the tropics and subtropics, with the tropical heating and subtropical cooling in D3 being much weaker than in the reanalysis. We believe that this is related to the general inability of idealized models to realistically simulate convective processes and associated latent heat releases in the tropics. This leads to a Hadley circulation that is too weak, as, for example, the tropical meridional winds in D3 are around 3 times slower than in the reanalysis (not shown). As a result, the meridional heat transports are also too weak, requiring relatively small diabatic heating terms to balance the energy and to create temperatures that resemble the observations. Another possible reason is that geostrophic balance and hence thermal wind relationship is not strictly valid in the tropics and thus that temperatures do not provide a sufficient constraint on the circulation.

Experiment D13 (Figure 5d) exhibits extratropical patterns of Q that are somewhat similar to the reanalysis but clearly not as good as in D3. This is indicative of a less realistic circulation in D13, with weaker eddies and associated heat transports, as the surface drag is presumably too large. Experiment CTR (Figure 5c) has almost no zonal variations in Q, which is not surprising given the zonally symmetric T_{eq}. The small variations in Q over the Northern Hemisphere are consistent with the use of a wave-2 orography.

4. Conclusion and Discussion

We construct and test an idealized general circulation model of the coupled stratosphere-troposphere system. The model is forced with Earth-like topography and zonally asymmetric equilibrium temperatures, which are determined by minimizing the RMS difference between observed and model-simulated 3-dimensional temperatures using an iterative procedure similar to that proposed by Chang (2006). Compared to previous idealized models, the new model has an improved atmospheric circulation at no extra computational costs. Similar to Chang (2006), the improvements concern the 3-dimensional wind structure and the diabatic forcing in the troposphere. The new outcomes of our study are improvements in the stratospheric circulation and variability, with a more realistic planetary wave spectrum and a higher frequency of SSWs than in previous idealized modeling studies. Other aspects of SSWs, like their downward influence into the troposphere, their persistence time scale, or the typical over-recovery of the vortex after SSWs (Hitchcock et al., 2013) are not considered here and will be addressed in future research.

A key-aspect of the new model is the use of zonally asymmetric equilibrium temperatures. The asymmetries are crucial for the generation of sufficient planetary wave activity and SSW events, despite the use of actual bottom topography. This is in contrast to previous idealized model studies, which use an unrealistically high-amplitude topography to create SSW events, albeit at a frequency which is still too low compared to the observations.

We note that our model does not have a parameterization for gravity wave drag. This drag has shown to be important for realistic simulations of the strength and variability of the polar vortex in complex models (e.g., Richter et al., 2010). In our model, the climatological effect of the drag is to some extent included in the equilibrium temperature profile, but some of the wind differences between reanalysis and our simulations may well be due to the missing gravity wave drag. Gravity wave drag may also play a role for the evolution and structure of SSWs, but this issue goes beyond the scope of our study.

We also test the sensitivity of our new model to the prescribed surface drag. For each value of the surface drag, we start a new iterative procedure to determine the optimal equilibrium temperatures. We find that increasing the magnitude of the surface drag reduces the stratospheric wave driving and thus the frequency of SSWs. In trying to determine the optimal value for the surface drag, we further find that there is no single value for the surface drag that is best in every respect. However, a drag of ~0.9 d^{-1} leads to overall best results, which is close to the original value of 1.0 d^{-1} of HS94.

An important lesson learned from this work is that the stratosphere contains a large amount of interannual to decadal variability (e.g., Figure 2), related to the aperiodic and extreme behavior of SSWs. Therefore, work that involves stratospheric effects requires long simulations to achieve statistically sound results. Theoretically, records of at least 400 years are needed to reduce the error in determining the SSW frequency to 10%, and caution must be exercised when constraining model simulations of stratospheric dynamics with the relatively short observational record.

We believe that our new model reduces the gap between traditional idealized model approaches on the one hand and complex climate models on the other hand. This is related to the improved circulation of the new model, something that may be important when trying to apply results from idealized modeling to more complex models. For example, the Polvani and Kushner (2002) model produces large shifts in the phase and amplitude of the stationary waves, and one needs to be cautious when interpreting the idealized modeling results (Smith et al., 2010). Another advantage of the new model is the use of a realistic topography, making it easier to prescribe to the model localized, climate-change-like forcings, such as changes in sea surface temperatures, sea ice, snow cover, or other effects. Our model can also be used to investigate the sensitivity of the circulation to global warming; this is achieved by replacing the reanalysis temperature climatology for the iterative procedure by the output from a full model for present and future climate. The new model also allows distinguishing between the large scale thermodynamic and surface drag effects of land and ocean and exploring effects that relate to these two surface types. At the same time, the new model has the same computational and methodological advantages as traditional idealized models, permitting the intensive study of sensitivities to parameters and idealized forcings. One cautionary note of the new model concerns the optimal choice of the surface drag coefficient, which might be resolution dependent; this should be tested before using different resolutions. In future work, we intend to use the new model to gain a more basic understanding for the factors that control the climatological frequency of SSWs.

Acknowledgments

We thank the two anonymous reviewers for their comments and suggestions. We thank the National Science Foundation (NSF) for providing support for this research under grant 1446292. We also thank the Center for High Performance Computing (CHPC) at the University of Utah for providing computational resources. We thank Sumant Nigam for providing to us the ERA-40 diabatic heating data. We also acknowledge the use of computational resources at the NCAR-Wyoming Supercomputing Center provided by NSF and the State of Wyoming and supported by NCAR's Computational and Information Systems Laboratory. We also thank NASA, NCEP/NCAR, and ECMWF for providing the Modern-Era Retrospective analysis for Research and Applications 2, NNR, and ERA-40 reanalysis. The interested reader can find the updated version of the GFDL dry dynamical core model along with the T_{eq} of the last iteration (31) of our "best" experiment D3 at https://github.com/ZhengWinnieWu/WR_simpleGCM.

References

Anderson, J. L., Balaji, V., Broccoli, A. J., Cooke, W. F., Delworth, T. L., Dixon, K. W., et al. (2004). The new GFDL global atmosphere and land model AM2-LM2: Evaluation with prescribed SST simulations. *Journal of Climate*, *17*(24), 4641–4673.

Baldwin, M. P., & Dunkerton, T. J. (2001). Stratospheric harbingers of anomalous weather regimes. *Science*, *294*(5542), 581–584. https://doi.org/10.1126/science.1063315

Becker, E., & Schmitz, G. (2003). Climatological effects of orography and land-sea heating contrasts on the gravity wave-driven circulation of the mesosphere. *Journal of the Atmospheric Sciences*, *60*(1), 103–118. https://doi.org/10.1175/1520-0469(2003)060%3C0103:CEOOAL%3E2.0.CO;2

Bosilovich, M. G., Lucchesi, R., & Suarez, M. (2016). MERRA-2: File specification. GMAO Office Note, No. 9 (Version 1.1), 73 pp, available from http://gmao.gsfc.nasa.gov/pubs/office_notes

Chan, S. C., & Nigam, S. (2009). Residual diagnosis of diabatic heating from ERA-40 and NCEP reanalyses: Intercomparisons with TRMM. *Journal of Climate*, *22*(2), 414–428. https://doi.org/10.1175/2008JCLI2417.1

Chang, E. K. M. (2006). An idealized nonlinear model of the northern hemisphere winter storm tracks. *Journal of the Atmospheric Sciences*, *63*(7), 1818–1839. https://doi.org/10.1175/JAS3726.1

Charlton, A. J., & Polvani, L. M. (2007). A new look at stratospheric sudden warmings. Part I: Climatology and modeling benchmarks. *Journal of Climate*, *20*(3), 449–469. https://doi.org/10.1175/JCLI3996.1

Charlton, A. J., Polvani, L. M., Perlwitz, J., Sassi, F., Manzini, E., Shibata, K., et al. (2007). A new look at stratospheric sudden warmings. Part II: Evaluation of numerical model simulations. *Journal of Climate*, *20*(3), 470–488. https://doi.org/10.1175/JCLI3994.1

Chen, G., Held, I. M., & Robinson, W. (2007). Sensitivity of the latitude of the surface westerlies to surface friction. *Journal of the Atmospheric Sciences*, *64*(8), 2899–2915. https://doi.org/10.1175/JAS3995.1

Chen, S. C., & Trenberth, K. E. (1988). Orographically forced planetary waves in the northern hemisphere winter: Steady state model with wave-coupled lower boundary formulation. *Journal of the Atmospheric Sciences*, *45*(4), 657–681. https://doi.org/10.1175/1520-0469(1988)045%3C0657:OFPWIT%3E2.0.CO;2

Dickinson, R. E. (1968). Planetary Rossby waves propagating vertically through weak westerly wind wave guides. *Journal of the Atmospheric Sciences*, *25*(6), 984–1002. https://doi.org/10.1175/1520-0469(1968)025%3C0984:PRWPVT%3E2.0.CO;2

Edmon, H. J., Hoskins, B. J., & McIntyre, M. E. (1980). Eliassen-Palm cross sections for the troposphere. *Journal of the Atmospheric Sciences*, *37*(12), 2600–2616. https://doi.org/10.1175/1520-0469(1980)037%3C2600:EPCSFT%3E2.0.CO;2

Eichelberger, S. J., & Hartmann, D. L. (2007). Zonal jet structure and the leading mode of variability. *Journal of Climate*, *20*(20), 5149–5163. https://doi.org/10.1175/JCLI4279.1

Eliassen, A., & Palm, E. (1961). On the transfer of energy in stationary mountain waves. *Geofysiske Publikasjoner*. https://doi.org/10.1098/rstl.1884.0016

Garfinkel, C. I., & Waugh, D. W. (2014). Tropospheric Rossby wave breaking and variability of the latitude of the eddy-driven jet. *Journal of Climate*, *27*(18), 7069–7085. https://doi.org/10.1175/JCLI-D-14-00081.1

Gerber, E. P., & Polvani, L. M. (2009). Stratosphere-troposphere coupling in a relatively simple AGCM: The importance of stratospheric variability. *Journal of Climate*, *22*(8), 1920–1933. https://doi.org/10.1175/2008JCLI2548.1

Held, I. M., & Suarez, M. J. (1994). A proposal for the intercomparison of the dynamical cores of atmospheric general circulation models. *Bulletin of the American Meteorological Society*, *75*(10), 1825–1830. https://doi.org/10.1175/1520-0477(1994)075%3C1825:APFTIO%3E2.0.CO;2

Held, I. M., Ting, M., & Wang, H. (2002). Northern winter stationary waves: Theory and modeling. *Journal of Climate*, *15*(16), 2125–2144. https://doi.org/10.1175/1520-0442(2002)015%3C2125:NWSWTA%3E2.0.CO;2

Hitchcock, P., Shepherd, T. G., Taguchi, M., Yoden, S., & Noguchi, S. (2013). Lower-stratospheric radiative damping and polar-night jet oscillation events. *Journal of the Atmospheric Sciences*, *70*(5), 1391–1408. https://doi.org/10.1175/JAS-D-12-0193.1

Jucker, M., Fueglistaler, S., & Vallis, G. K. (2013). Maintenance of the stratospheric structure in an idealized general circulation model. *Journal of the Atmospheric Sciences*, *70*(11), 3341–3358. https://doi.org/10.1175/JAS-D-12-0305.1

Jucker, M., Fueglistaler, S., & Vallis, G. K. (2014). Stratospheric sudden warmings in an idealized GCM. *Journal of Geophysical Research*, *119*, 11,054–11,064. https://doi.org/10.1002/2014JD022170

Kalnay, E., Kanamitsu, M., Kistler, R., Collins, W., Deaven, D., Gandin, L., et al. (1996). The NCEP/NCAR 40-year reanalysis project. *Bulletin of the American Meteorological Society*, *77*(3), 437–471. https://doi.org/10.1175/1520-0477(1996)077%3C0437:TNYRP%3E2.0.CO;2

Kushner, P., & Polvani, L. M. (2004). Stratosphere-troposphere coupling in a relatively simple AGCM: The role of eddies. *Journal of Climate*, *17*(3), 629–639. https://doi.org/10.1175/1520-0442(2004)017%3C0629:SCIARS%3E2.0.CO;2

Limpasuvan, V., & Hartmann, D. L. (2000). Wave-maintained annular modes of climate variability. *Journal of Climate*, *13*(24), 4414–4429. https://doi.org/10.1175/1520-0442(2000)013%3C4414:WMAMOC%3E2.0.CO;2

Matsuno, T. (1971). A dynamical model of the stratospheric sudden warming. *Journal of the Atmospheric Sciences*, *28*(8), 1479–1494. https://doi.org/10.1175/1520-0469(1971)028%3C1479:ADMOTS%3E2.0.CO;2

Mcintyre, E. (1982). How well do we understand the dynamics of stratospheric warmings by Michael E. McIntyre Department of Applied Mathematics and Theoretical Physics, University of Cambridge, U. K. (manuscript received 19 October 1981) Abstract. *Journal of the Meteorological Society of Japan*, *60*(February), 37–65.

Polvani, L. M., & Kushner, P. (2002). Tropospheric response to stratospheric degradation in a simple global circulation model. *Journal of the Atmospheric Sciences*, *29*(15), 1835–1846.

Polvani, L. M., & Waugh, D. W. (2004). Upward wave activity flux as a precursor to extreme stratospheric events and subsequent anomalous surface weather regimes. *Journal of Climate*, *17*(18), 3548–3554. https://doi.org/10.1175/1520-0442(2004)017%3C3548:UWAFAA%3E2.0.CO;2

Reichler, T., Kushner, P. J., & Polvani, L. M. (2005). The coupled stratosphere-troposphere response to impulsive forcing from the troposphere. *Journal of the Atmospheric Sciences*, *62*(9), 3337–3352. https://doi.org/10.1175/JAS3527.1

Richter, J. H., Sassi, F., & Garcia, R. R. (2010). Toward a physically based gravity wave source parameterization in a general circulation model. *Journal of the Atmospheric Sciences*, *67*(1), 136–156. https://doi.org/10.1175/2009JAS3112.1

Sheshadri, A., Plumb, R. A., & Gerber, E. P. (2015). Seasonal variability of the polar stratospheric vortex in an idealized AGCM with varying tropospheric wave forcing. *Journal of the Atmospheric Sciences*, *72*(6), 2248–2266. https://doi.org/10.1175/JAS-D-14-0191.1

Smith, K. L., Fletcher, C. G., & Kushner, P. J. (2010). The role of linear interference in the annular mode response to extratropical surface forcing. *Journal of Climate*, *23*(22), 6036–6050. https://doi.org/10.1175/2010JCLI3606.1

Thompson, D. W. J., Baldwin, M. P., & Wallace, J. M. (2002). Stratospheric connection to Northern Hemisphere wintertime weather: Implications for prediction. *Journal of Climate*, *15*(12), 1421–1428. https://doi.org/10.1175/1520-0442(2002)015%3C1421:SCTNHW%3E2.0.CO;2

Uppala, S. M., Kållberg, P. W., Simmons, A. J., Andrae, U., da Costa Bechtold, V., Fiorino, M., et al. (2005). The ERA-40 re-analysis. *Quarterly Journal of the Royal Meteorological Society*, *131*(612), 2961–3012. https://doi.org/10.1256/qj. 04.176

Wu, Y., & Smith, K. L. (2016). Response of Northern Hemisphere midlatitude circulation to arctic amplification in a simple atmospheric general circulation model. *Journal of Climate*, *29*(6), 2041–2058. https://doi.org/10.1175/JCLI-D-15-0602.1